SCIENCE CHINA
Information Sciences

• **Supplementary File** •

Dielectric Metasurface Enhanced Performance in Multilayer WS_2 Photodetector

Huijuan Zhao[1], Weiqi Wang[1], Huanlin Ding[1], Sumei Wang[2], Zemin Tang[1], Shuhan Li[1], Jiaxuan Wang[1], Yufan Wang[1], Qiyuan Zhou[1], Anran Wang[2], Yuanfang Yu[1] and Li Gao[1,2*]

[1]*State Key Laboratory of Flexible Electronics (LoFE) & Institute of Advanced Materials (IAM), Nanjing University of Posts & Telecommunications, 9 Wenyuan Road, Nanjing 210023, China.*

[2]*School of Science, Nanjing University of Posts and Telecommunications, Nanjing 210023, China.*

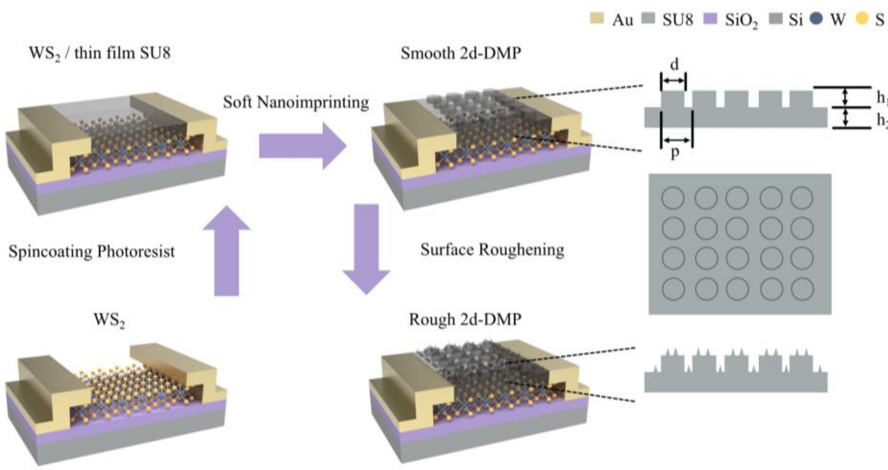

Figure S1 Schematic illustration of the structured SU8 metasurface on a WS_2 photodetector (2d-DMP) and its fabrication process. The SU8 cylinders have a diameter d (620 nm) and a periodicity p (1020 nm), where h_1 (330 nm) represents the height of the nanocylinders, and h_2 (300 nm) indicates the thickness of the underlying SU8 layer, as depicted in the diagram.

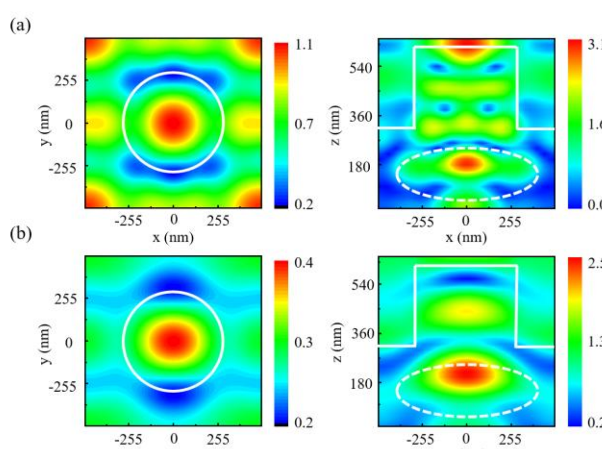

Figure S2 FDTD electric field simulation. (a) Top view and cross-section view of electric field simulation for a h_2 layer thickness of 250 nm. (b) Top view and cross-section view of electric field simulation for an h_2 layer thickness of 350 nm.

*Correspondingauthor(email: iamlgao@njupt.edu.cn)

The electric field distribution of h_2 at different thicknesses was simulated based on the FDTD method (FDTD Solutions, Lumerical, Canada), using plane wave normal incidence. The electric field enhancement effect is best when h_2 is 300 nm.

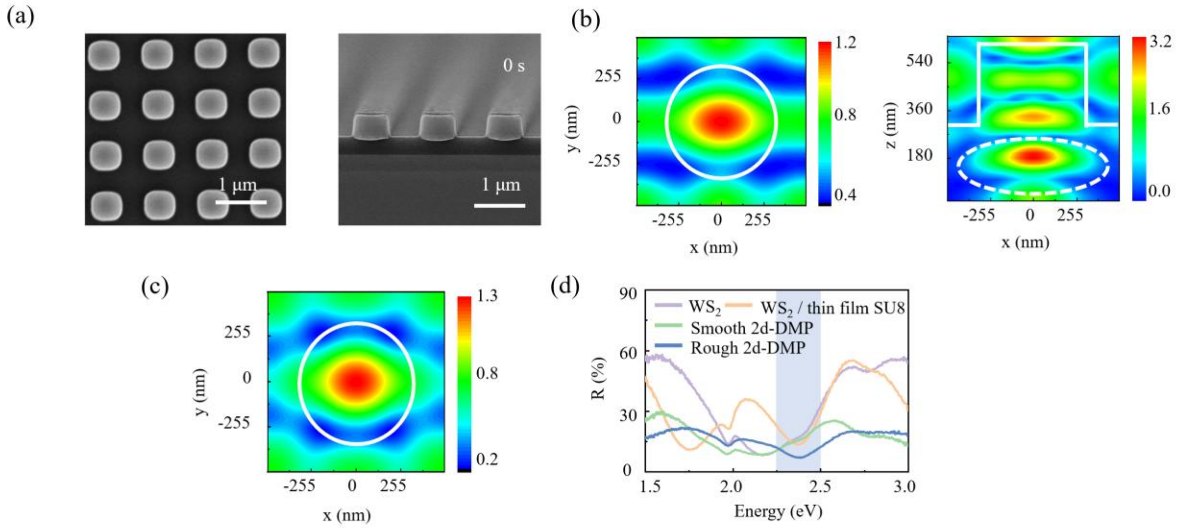

Figure S3 (a) The SEM of structured SU8 metasurface. The top view (left) and cross-section view (right) depict a cylindrical periodic structure. (b) FDTD simulation of the electric field distribution after 0 seconds of RIE treatment. (c) FDTD simulation of the electric field distribution after 60 seconds of RIE treatment. (d) Reflection R.

The optimal structural parameters were determined through FDTD simulations. The structure was then patterned on the SU8 photoresist film through nanoimprinting, as illustrated in Figure S3(a). To create a nanoscale structured SU8 metasurface on the multilayer WS_2, an SU8 thin film was prepared via spin-coating, followed by soft nanoimprinting to construct the desired structures. SU8 photoresist (SU8-2000, MicroChem) was diluted in cyclopentanone at a ratio of 1:1. Using a spin coater (Easycoater6), an approximately 600 nm thick SU8 film was spin-coated onto the surface of the multilayer WS_2 at a speed of 4000 rpm and an acceleration of 300 r/s^2 for 30 seconds, ensuring uniform film thickness. The photoresist solution concentration and the spin coating speed can be adjusted to achieve different photoresist thin film thicknesses, which affect the final vertical cavity dimension. After the spin-coating of the SU8 film was completed, pre-made polydimethylsiloxane (PDMS) mold was pressed directly onto the SU8 film. The silicon template of the target structure was placed in the vacuum environment of "1H,1H,2H,2H-perfluoro octyl trichlorosilane" reagent for 2 hours, and then the configured hard-PDMS was slowly covered on the silicon template, and then the hard-PDMS on the surface of the silicon template was uniformly blown with a nitrogen gun to form a thin layer and cover the entire surface of the silicon wafer. The soft-PDMS coating was prepared in a ratio of 10:1 and stirred until creamy, then the soft-PDMS was completely covered with the hard-PDMS layer, then placed in a vacuum drying oven and left for 2 hours until the air bubbles in the material were completely removed, and then place in an oven at 75 ℃ for 20 minutes to completely cure the PDMS and form the mold. The thermal imprinting process was carried out at 65 ℃ and 90 ℃ for 1 minute each, replicating a cylindrical nanostructure with a diameter of 620 nm, a period of 1020 nm, and a height of 330 nm on the SU8 surface. Figure S3(b) shows the top view and cross-sectional view of the electric field distribution after structuring, and Figure S3(c) and Figure 1(c) shows the top view and cross-sectional view of the electric field distribution after roughening the structure by etching with RIE for 60 seconds. As demonstrated by Liu et al, smaller texture sizes typically result in an increased number of scatterings and reflections of light. The scattering process can cause a change in the direction of light propagation, thereby allowing more light to enter the material. Furthermore, when light is reflected multiple times off a surface, the effective propagation path is lengthened, and the light remains inside the material for a longer period. Concurrently, the structure concentrates the electric field of the light, particularly at recessed sections or acute vertices, resulting in the formation of localized electric field enhancement zones. This enhancement effect improves the interaction between light and the material, thereby enhancing the absorption of light[1, 2] , as shown in Figure S3(d).

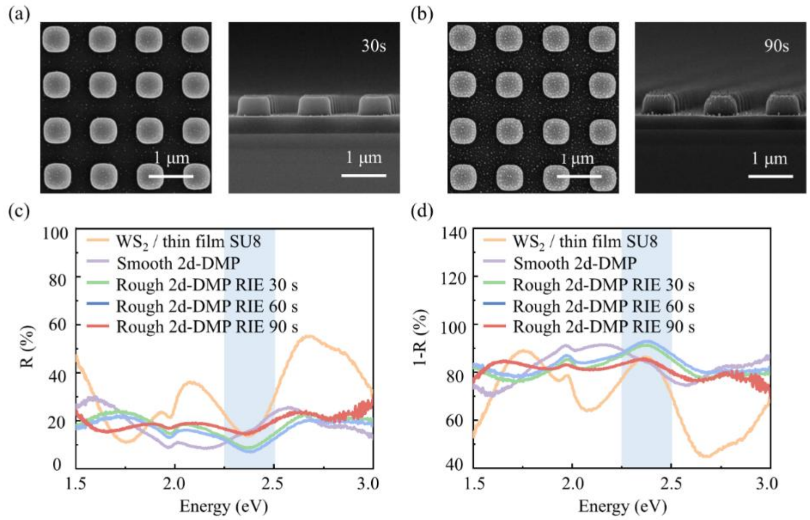

Figure S4 Morphological characterization and spectral analysis of structured SU8 metasurfaces etched for different times. (a) Scanning electron microscope image of the metasurface after 30s of RIE etching. (b) Scanning electron microscope image of the metasurface after 90s of RIE etching. (c) Reflection R. (d) Rough representation of absorption 1-R.

At the 30-second mark, some minor imperfections emerge, as shown in Figure S4(a). The thickness of the SU8 film h_2 is approximately 300 nm, indicating that the introduction of roughness and the absorption enhancement are not yet optimized. Upon extending the time t to 90 s, as shown in Figure S4(b). The thickness of the SU8 film h_2 is approximately 230 nm, and the structural parameters exhibit a significant deviation from the optimal values obtained from the simulation. It becomes evident that the overall performance is compromised as excessive etching destroys the cavity mode at target wavelengths. As illustrated in Figure S4(c)-(d), the absorption effects markedly diminished. A significant change in the thickness of the microcavity will impact the resonance and light trapping efficiency of the structure, leading to a reduction in the absorption of photons in the two-dimensional material.As a result, the electric field enhancement effect, which is crucial for improving optoelectronic performance, will not be fully realized.

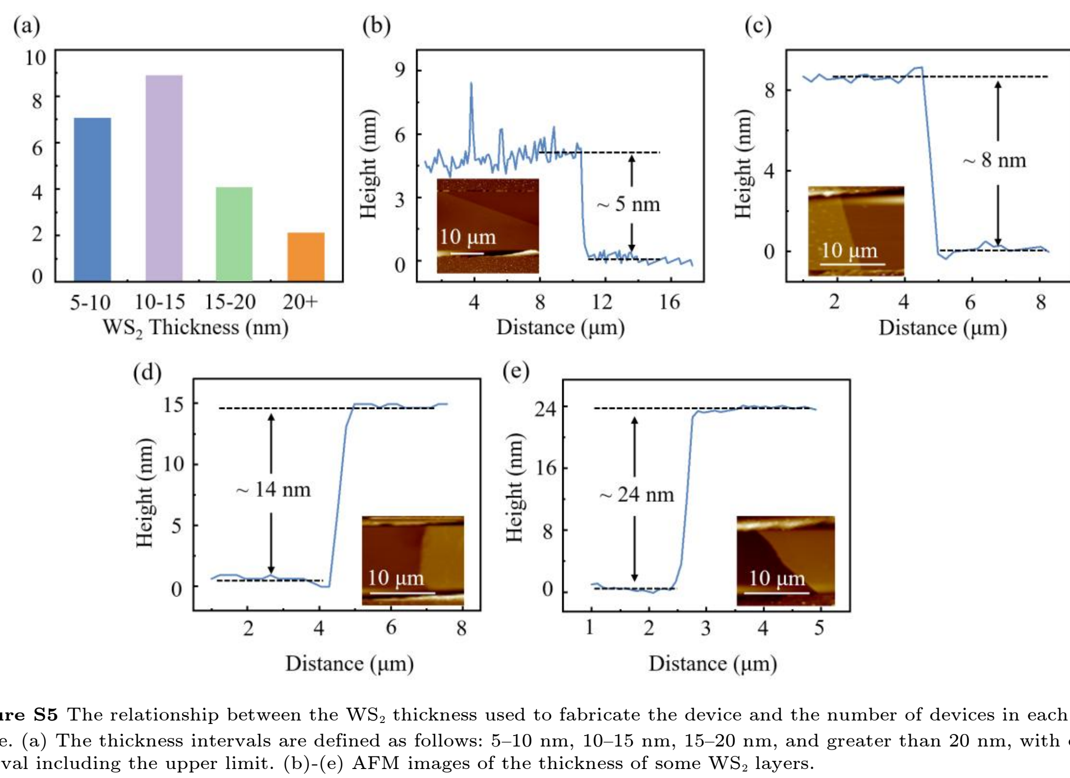

Figure S5 The relationship between the WS_2 thickness used to fabricate the device and the number of devices in each thickness range. (a) The thickness intervals are defined as follows: 5–10 nm, 10–15 nm, 15–20 nm, and greater than 20 nm, with each interval including the upper limit. (b)-(e) AFM images of the thickness of some WS_2 layers.

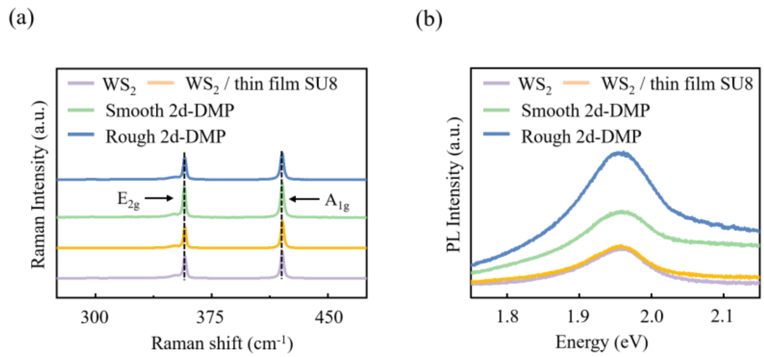

Figure S6 (a) Raman spectra of multi-layer WS_2, WS_2 / thin- film SU8, Smooth 2d-DMP, and Rough 2d-DMP. (b) PL spectra of multi-layer WS_2, WS_2 / thin- film SU8, Smooth 2d-DMP, and Rough 2d-DMP.

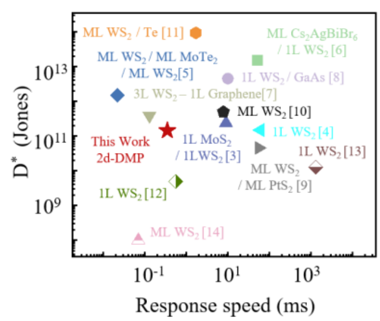

Figure S7 Performance Comparison of Various Devices[3-14].

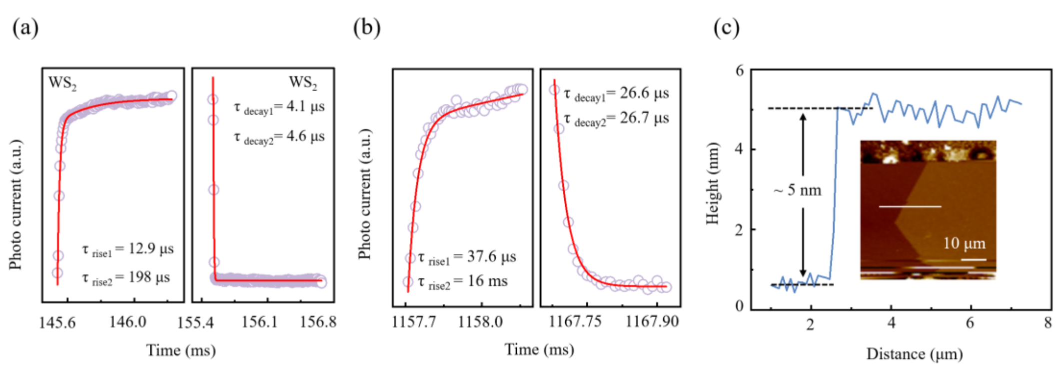

Figure S8 (a) The transient response of the WS_2 photodetector. (b) The transient response of the WS_2 photodetector whose silicon oxide surface is not treated with oxygen. (c) AFM characterization of multilayer WS_2, the WS_2 photodetector whose silicon oxide surface is not treated with oxygen. The height profile indicates a thickness of approximately 5 nm.

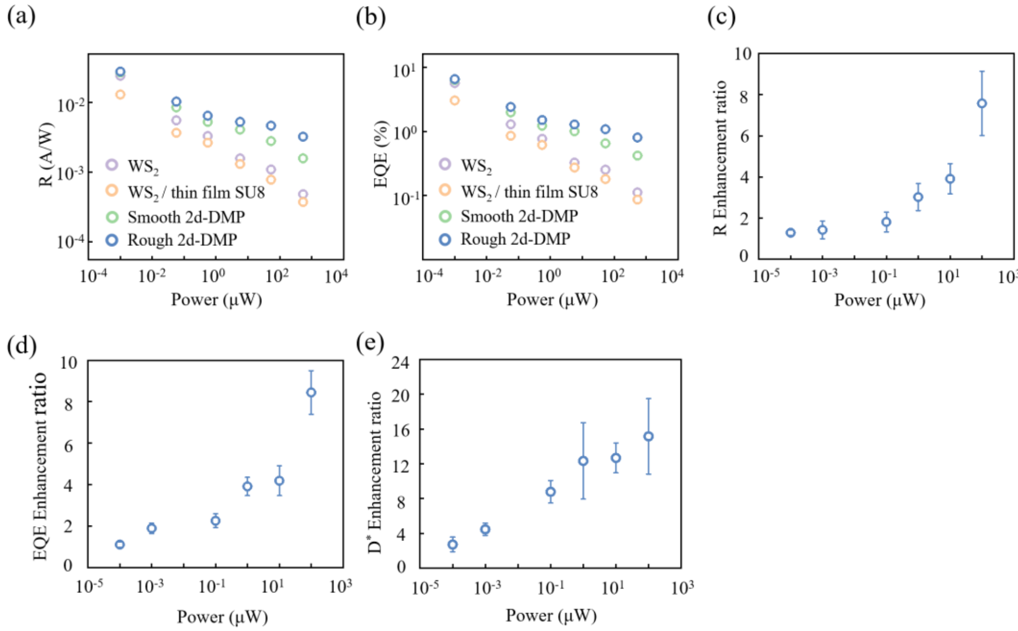

Figure S9 (a-b) R and EQE of multi-layer WS_2, WS_2 / thin film SU8, smooth 2d-DMP, and rough 2d-DMP. (c) R enhancement ratio as a function of incident power, illustrating the enhancement of R after structuring at different power intensities. (d) EQE enhancement ratio as a function of incident power, illustrating the enhancement of EQE after structuring at different power intensities. (e) D* enhancement ratio as a function of incident power, illustrating the enhancement of D* after structuring at different power intensities.

References

1 Liu J, He Y, Ding L, et al. Perovskite/silicon tandem solar cells with bilayer interface passivation Nature, 2024, 635: 596-603

2 Clapham P B, Hutley M C. Reduction of Lens Reflexion by the “Moth Eye” Principle. Nature, 1973, 244: 281-282

3 Lin X, Wang F, Shan X, et al. High-performance photodetector and its optoelectronic mechanism of MoS_2/WS_2 vertical heterostructure. Applied Surface Science, 2021, 546: 149074

4 Zhang S, Hao Y, Gao F, et al. Controllable growth of wafer-scale two-dimensional WS_2 with outstanding optoelectronic properties. 2D Materials, 2024, 11: 015007

5 Wu Z, Chen M, Liu X, et al. Sandwiched $WS_2/MoTe_2/WS_2$ Heterostructure with a Completely Depleted Interlayer for a Photodetector with Outstanding Detectivity. ACS Applied Materials & Interfaces, 2024, 16: 36609-36619

6 Fang F, Wan Y, Li H, et al. Two-Dimensional $Cs_2AgBiBr_6/WS_2$ Heterostructure-Based Photodetector with Boosted Detectivity via Interfacial Engineering. ACS Nano, 2022, 16: 3985-3993

7 Mehew J D, Unal S, Torres Alonso E, et al. Fast and Highly Sensitive Ionic-Polymer-Gated WS_2–Graphene Photodetectors. Advanced Materials, 2017, 29: 1700222

8 Li K, Wang W, Li J, et al. High-responsivity, self-driven photodetectors based on monolayer WS_2/GaAs heterojunction. Photon Res, 2020, 8: 1368-1374

9 Wang Z, Zhang H, Wang W, et al. Type-I Heterostructure Based on WS_2/PtS_2 for High-Performance Photodetectors. ACS Applied Materials & Interfaces, 2022, 14: 37926-37936

10 Gao W, Zhang S, Zhang F, et al. 2D WS_2 Based Asymmetric Schottky Photodetector with High Performance. Advanced Electronic Materials, 2021, 7: 2000964

11 Luo Z, Xu H, Gao W, et al. High-Performance and Polarization-Sensitive Imaging Photodetector Based on WS_2/Te Tunneling Heterostructure. Small, 2023, 19: 2207615

12 Lan C, Zhou Z, Zhou Z, et al. Wafer-scale synthesis of monolayer WS_2 for high-performance flexible photodetectors by enhanced chemical vapor deposition. Nano Research, 2018, 11: 3371-3384

13 Aggarwal P, Kaushik S, Bisht P, et al. Centimeter-Scale Synthesis of Monolayer WS_2 Using Single-Zone Atmospheric-Pressure Chemical Vapor Deposition: A Detailed Study of Parametric Dependence, Growth Mechanism, and Photodetector Properties. Crystal Growth & Design, 2022, 22: 3206-3217

14 Quereda J, Kuriakose S, Munuera C, et al. Scalable and low-cost fabrication of flexible WS_2 photodetectors on polycarbonate. npj Flexible Electronics, 2022, 6: 23